A&A 413, 681–691 (2004)
DOI: 10.1051/0004-6361:20034326

Astronomy & Astrophysics

The spatial structure of the β Pictoris gas disk⋆

A. Brandeker[1], R. Liseau[1], G. Olofsson[1], and M. Fridlund[2]

[1] Stockholm Observatory, AlbaNova University Centre, 106 91 Stockholm, Sweden
e-mail: rene@astro.su.se, olofsson@astro.su.se
[2] ESA/ESTEC, PO Box 299, 2200 AG Noordwijk, The Netherlands
e-mail: Malcolm.Fridlund@esa.int

Received 17 September 2003 / Accepted 7 October 2003

Abstract. We have used VLT/UVES to spatially resolve the gas disk of β Pictoris. 88 extended emission lines are observed, with the brightest coming from Fe I, Na I and Ca II. The extent of the gas disk is much larger than previously anticipated; we trace Na I radially from 13 AU out to 323 AU and Ca II to heights of 77 AU above the disk plane, both to the limits of our observations. The degree of flaring is significantly larger for the gas disk than the dust disk. A strong NE/SW brightness asymmetry is observed, with the SW emission being abruptly truncated at 150–200 AU. The inner gas disk is tilted about 5° with respect to the outer disk, similar to the appearance of the disk in light scattered from dust. We show that most, perhaps all, of the Na I column density seen in the "stable" component of absorption, comes from the extended disk. Finally, we discuss the effects of radiation pressure in the extended gas disk and show that the assumption of hydrogen, in whatever form, as a braking agent is inconsistent with observations.

Key words. stars: individual: β Pictoris – stars: circumstellar matter – stars: planetary systems: formation – stars: planetary systems: protoplanetary disks

1. Introduction

The young, near-by main-sequence star β Pictoris has been the subject of intense studies ever since it was discovered to harbour circumstellar cold dust (Aumann 1985), distributed along a linear shape (Smith & Terrile 1984), interpreted as a "debris disk" (Backman & Paresce 1993). These studies have been largely motivated by the possibility of observing an analogue to the solar system in its early stages, in the hope of finding clues to the mechanisms of planet formation. Asymmetries found in the disk from light *scattered* by the dust (Kalas & Jewitt 1995; Heap et al. 2000) have indeed been suggested to be the signature of perturbing planet(s) (Moulliet et al. 1997; Augereau et al. 2001), but so far no direct detection of a planet around β Pic has been made. Asymmetries have also been detected in *thermal emission* from the dust (Liseau et al. 2003; Weinberger et al. 2003 with references therein). Recent papers reviewing the β Pic disk are those by Artymowicz (2000), Lagrange et al. (2000) and Zuckerman (2001).

Circumstellar *gas*, seen in absorption against the star, was also found early on (Hobbs et al. 1985), thanks to the favourable edge-on orientation of the disk. Finding and characterising the gas content is important for understanding its relation to the dust and the general evolution of the disk (Artymowicz 2000). Gas is also useful as a probe of physical conditions in the disk, where density, composition, temperature and bulk velocities under favourable conditions can be directly estimated.

The gas found at relative rest to β Pic, consisting of metals, raised the problem why it is not blown away from the system by the high radiation pressure. Lagrange et al. (1998) made some detailed calculations and found that the gas drag from a dense enough H I ring ($n_{\rm H\,I} \geq 10^5\,{\rm cm}^{-3}$) close to the star (~0.5 AU) could brake migrating particles sufficiently, provided they started out inside the ring. The picture was complicated by the announcement of H_2 detected in emission by the Infrared Space Observatory (Thi et al. 2001), implying large quantities (~50 $M_\oplus$) of molecular hydrogen, and the subsequent report of sensitive upper limits ($N(H_2) \lesssim 10^{18}\,{\rm cm}^{-2}$) of H_2 from FUV absorption lines using β Pic as a background source (Lecavelier des Etangs et al. 2001). In addition, Olofsson et al. (2001, hereafter Paper I) found spatially resolved widespread gas emission from Na I in the disk, stretching out to at least 140 AU.

Here we present observations improved by a factor of two in both spatial and spectral resolution, as well as a greatly increased spectral coverage, compared to Paper I. We put emphasis on the observed spatial structure of the gas disk, derive an empirical density profile of Na I atoms and use a photoionisation code to construct disk models consistent with our observations. We discuss implications of the radiation pressure under various conditions derived from these models. Results from a

Send offprint requests to: A. Brandeker,
e-mail: alexis@astro.su.se

⋆ Based on observations collected at the European Southern Observatory, Chile.

Table 1. VLT/UVES observation log.

UT Date	β Pic[a]	Grating[b]	Width[c]	Length[c]	Offset[d]	Orientation[d]	Exposures
2001-12-02 T 03:38	ON	437	0.″4	10″	–4.″4	Parallel	69 × 15 s
2001-12-02 T 03:38	ON	860	0.″3	12″	–4.″4	Parallel	47 × 25 s
2001-12-02 T 05:31	ON	390	0.″4	8″	–3.″4	Parallel	62 × 20 s
2001-12-02 T 05:31	ON	580	0.″3	12″	–3.″4	Parallel	48 × 25 s
2002-01-03 T 06:21	ON	390	0.″4	8″	–3.″4	Parallel	62 × 20 s
2002-01-03 T 06:21	ON	580	0.″3	12″	–3.″4	Parallel	48 × 25 s
2002-01-06 T 05:51	OFF	390	0.″4	8″	–3.″0	Orthogonal	3 × 1205 s
2002-01-06 T 05:51	OFF	580	0.″3	12″	–3.″0	Orthogonal	3 × 1195 s
2002-01-16 T 02:47	OFF	390	0.″4	8″	–11″	Parallel	3 × 1205 s
2002-01-16 T 02:47	OFF	580	0.″3	12″	–11″	Parallel	3 × 1195 s
2002-01-16 T 03:51	OFF	390	0.″4	8″	–6.″0	Orthogonal	3 × 1205 s
2002-01-16 T 03:51	OFF	580	0.″3	12″	–6.″0	Orthogonal	3 × 1195 s
2002-01-19 T 03:11	ON	390	0.″4	8″	3.″4	Parallel	62 × 20 s
2002-01-19 T 03:11	ON	580	0.″3	12″	3.″4	Parallel	48 × 25 s
2002-01-19 T 04:25	ON	390	0.″4	8″	3.″4	Parallel	62 × 20 s
2002-01-19 T 04:25	ON	580	0.″3	12″	3.″4	Parallel	48 × 25 s
2002-02-09 T 03:55	OFF	390	0.″4	8″	3.″0	Orthogonal	3 × 1205 s
2002-02-09 T 03:55	OFF	580	0.″3	12″	3.″0	Orthogonal	3 × 1195 s
2002-02-10 T 03:19	OFF	390	0.″4	8″	11″	Parallel	3 × 1205 s
2002-02-10 T 03:19	OFF	580	0.″3	12″	11″	Parallel	3 × 1195 s
2002-02-11 T 04:04	OFF	390	0.″4	8″	6.″0	Orthogonal	3 × 1205 s
2002-02-11 T 04:04	OFF	580	0.″3	12″	6.″0	Orthogonal	3 × 1195 s
2002-09-24 T 08:09	OFF	437	0.″4	10″	–3.″0	Orthogonal	3 × 1205 s
2002-09-24 T 08:09	OFF	860	0.″3	12″	–3.″0	Orthogonal	3 × 1195 s

[a] ON means that the star was inside the spectroscopic slit, OFF that it was outside.
[b] The gratings correspond to the following wavelength ranges: 326–445 nm for grating 390, 373–499 nm for grating 437, 476–684 nm for grating 580, and 660–1060 nm for grating 860.
[c] Width and length refer to the dimensions of the slit.
[d] Offset is the centre of the slit relative to β Pic in the plane of the disk, where positive offsets are to the north-east. The orientation of the slit is relative to the disk plane.

detailed study of the observed chemical abundances will be discussed in a forthcoming paper.

2. Observations

The star β Pictoris was observed with the echelle spectrograph UVES on the 8.2 m Kueyen telescope at the Very Large Telescope of ESO, Paranal, Chile. The observations were made in service mode to take advantage of the excellent seeing conditions occasionally provided by the site. Service mode means that the observers prepare observation blocks that are executed by the local telescope operators provided certain conditions (like air mass and seeing) are met. A total of 12 observation blocks during 2001–2002 (see Table 1) lasting about an hour each were successfully executed. The air mass and seeing at zenith were always below 1.5 and 0.″6, respectively. The UVES spectrograph was used in standard dichroic modes, meaning that a dichroic mirror was used to split the light into two wavelength ranges, each using its own echelle grating and CCD detectors. Two types of gratings were used for each arm, together covering the wavelengths 3300 Å to 10 400 Å with a spectral resolution ranging from $R \sim 80\,000$ in the blue to $R \sim 110\,000$ in the red. The blue arm was equipped with a single CCD of type EEV 44-82 and size 4096 × 4096 pixels, while the red arm had a mosaic of two CCDs of sizes 2048 × 4096 each, of the types EEV 44-82 and MIT-LL CCID-20. The spectroscopic slits were 0.″4 and 0.″3 wide in the blue and red arm, respectively. To adequately separate the echelle orders, slits were restricted to lengths between 8″ and 12″, depending on setting (see Table 1). Slits were positioned at 4 overlapping locations along the β Pic dust disk, and at 4 locations orthogonal to the disk, reaching a distance of 17″ from the star in the disk plane, and a height of 6″ above the plane (see Fig. 1). From the data, we determined the positioning of the slits, with respect to β Pic, to be better than ∼0.″2. Calibration data (flat-fields, bias frames, Th-Ar lamp wavelength calibration spectra, flux standard stars, etc.) were provided by the UVES calibration plan.

3. Data reduction

3.1. Pipeline reduction

The data were reduced using a modified version of the UVES pipeline 1.2, that runs in the ESO MIDAS environment. The pipeline automatically generates the appropriate calibration

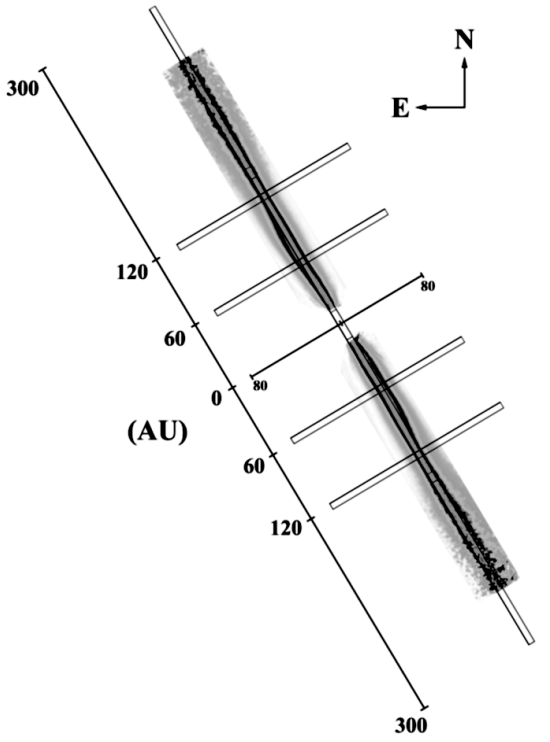

Fig. 1. Orientations and positions of the 8 different slit settings used. The background image shows observations of the dust as obtained by HST/STIS (Heap et al. 2000).

sets from the calibration data obtained as a part of the UVES calibration plan, and apply them to the science frames. The raw frames are bias subtracted, flat-fielded, background subtracted, order extracted, and wavelength calibrated. An error was corrected in the pipeline version 1.2, that associated a wavelength calibration to the wrong order when 2D extraction was selected without merging the orders.

The orders of the echelle grating are slightly inclined on the CCD with respect to pixel columns. Since the observations with the star on slit were performed under excellent seeing (the seeing measured in the spectra was $\sim$0.″7), this resulted in a very high flux gradient between the pixels on and off the star. By default, the orders are resampled linearly, but this caused the spectrum to show a periodic "spiky" pattern in the flux. We found that linear interpolation does not work properly due to the strong non-linear shape of the point spread function (PSF) at the pixel resolution. By modifying the order extracting routine to use a third order Catmull-Rom spline interpolation instead of linear, we found the spikes to be greatly reduced (though not completely eliminated).

The reduction procedure was complicated by the sheer load of data. With about 600 spectra, each 4096×4096 pixels, plus calibration frames etc., the raw data were close to 50 GB.

The end product of the pipeline reduction consisted of individual orders separated into individual files with the spatial information along the slit preserved, and a wavelength calibration guaranteed to be better than 0.5 km s^{-1}.

3.2. PSF subtraction

To trace the circumstellar gas emission as close as possible to the star, we had to subtract the scattered light from the star, in the cases where the star was in the slit. To do this, we estimated the stellar spectrum S by centering a small aperture on the star. To allow for slow gradients, we took advantage of the fact that the gas emission lines are narrow (a few pixels) and produced a median filtered version M of the stellar spectrum S, using a window of 30–60 pixels. We also obtained the median filtered spectrum m_i at each spatial position i, using the same median filter window. The stellar PSF subtracted spectrum was then estimated as $s_i = r_i - m_i S/M$, where r_i is the spectrum at position i. For the observations where the star was off the slit, we just subtracted the median filtered background scattered light (scattered both locally by the dust disk and in the atmosphere / telescope), $s_i = r_i - m_i$.

3.3. Flux calibration

To flux-calibrate the data, we made use of the master response curves provided by the UVES team. The master response curves are generated from long-time monitoring of the sensitivity trends of the instrument, and are provided for various standard settings and periods in time. The claimed absolute flux calibration is 10%, but comparing with standard flux stars observed (with an open slit) the same nights as β Pic we found the derived fluxes to deviate by as much as 40% from tabulated values for these stars. We thus used the master response curves to correct only for the over-all sensitivity dependence on wavelength, and used the standard star spectra obtained in connection with the β Pic observations to correct the absolute flux calibration. By looking at the variations of the derived absolute fluxes of disk emission lines observed several times, we estimate that the error on the absolute flux is about 5–10%. Since we use a narrow slit (0.″3–0.″4), the slit losses from a point source like β Pic are substantial and very seeing dependent. The error of the absolute flux from the star is therefore expected to be substantially higher. Our main concern, however, is the flux of the disk emission, which, due to its spatial extension, is much more stable with regard to seeing variations.

3.4. Heliocentric wavelength correction

The wavelength calibration obtained from the UVES pipeline does not correct for the velocity of the instrument relative to the centre of the Sun. To transform the observed spectrum to a heliocentric frame, we made use of the software program RV written by P. T. Wallace and C. A. Clayton[1]. The obtained accuracy in the transformation is better than 0.01 km s^{-1}, fully adequate for our purposes.

3.5. Line flux measurements

From the reduced, PSF subtracted and wavelength calibrated spectra, the disk emission lines were measured in several steps.

[1] RV is available from `http://star-www.rl.ac.uk`

First the lines were identified by correlating their measured wavelengths with the atomic line database provided by NIST[2]. This procedure was greatly simplified by the high accuracy of the wavelength calibration, better than 0.5 km s^{-1}, corresponding to 0.01 Å at 6000 Å. A median systematic velocity was then calculated for the brightest and most accurately measured emission lines, assuming all shared the same systematic radial velocity. For the brightest lines, the measured flux as a function of apertures centred on the systematic velocity was evaluated. A large aperture samples more signal, but also more noise. We were therefore interested in finding the best balance, in order to achieve the highest signal to noise (S/N). The apertures used to measure emission lines were consequently chosen as a function of line strength and background noise, with smaller apertures for fainter lines. We assumed that all lines from a particular ion share the same spatio-spectral profile, and scaled the flux measured in small apertures of fainter lines with the ratio between equally sized and maximum sized apertures placed on the sum of several bright lines. In this way we estimated the signal from a faint line without integrating up too much noise. The method is analogous to methods used in aperture photometry to measure star fluxes in, e.g., a CCD image.

For the slits placed orthogonally to the disk, we summed up all flux in the spatial direction, i.e. along the height of the disk (Table 2). The quantity thus derived has the unit of flux per arcsecond.

4. Results

We detected 88 spatially extended emission lines from the β Pic gas disk, identified as emission from Fe I, Na I, Ca II, Ni I, Ni II, Ti I, Ti II, Cr I and Cr II. Table 2 shows a selection of the brightest lines. Following the brightest emission lines ($S/N \sim 50$) from Na I and Fe I radially (Figs. 2 and 3), we observe a strong asymmetry between the north-east (NE) and the south-west (SW) parts of the disk, similar to the brightness asymmetry in the dust emission (Kalas & Jewitt 1995), but asymmetric to a much higher degree. The NE gas emission extends smoothly to the limits of our observations (17″, corresponding to 330 AU at the distance of β Pic), whereas the SW emission is abruptly truncated at 150–200 AU. In the inner regions, the SW emission dominates over the NE part, in agreement with Fig. 2 of Paper I.

Determining the centre of emission from the orthogonal profiles, it becomes apparent that the inner part of the disk is slightly tilted with respect to the outer parts, in particular on the NE side (Fig. 4). We estimate this tilt to be $5° \pm 2°$ (1σ), similar to the 4°–5° tilt observed by HST/STIS in the inner dust disk (Heap et al. 2000).

The scale height ($FWHM$) of the gas disk, estimated on observations deconvolved with a Gaussian of 0.″7 to simulate the seeing, is ∼20 AU at 3″ (58 AU), similar to the dust disk scale height (Heap et al. 2000). At 6″ (116 AU), however, the gas disk is significantly thicker, ∼30 AU compared to ∼15 AU for the dust (see Fig. 5).

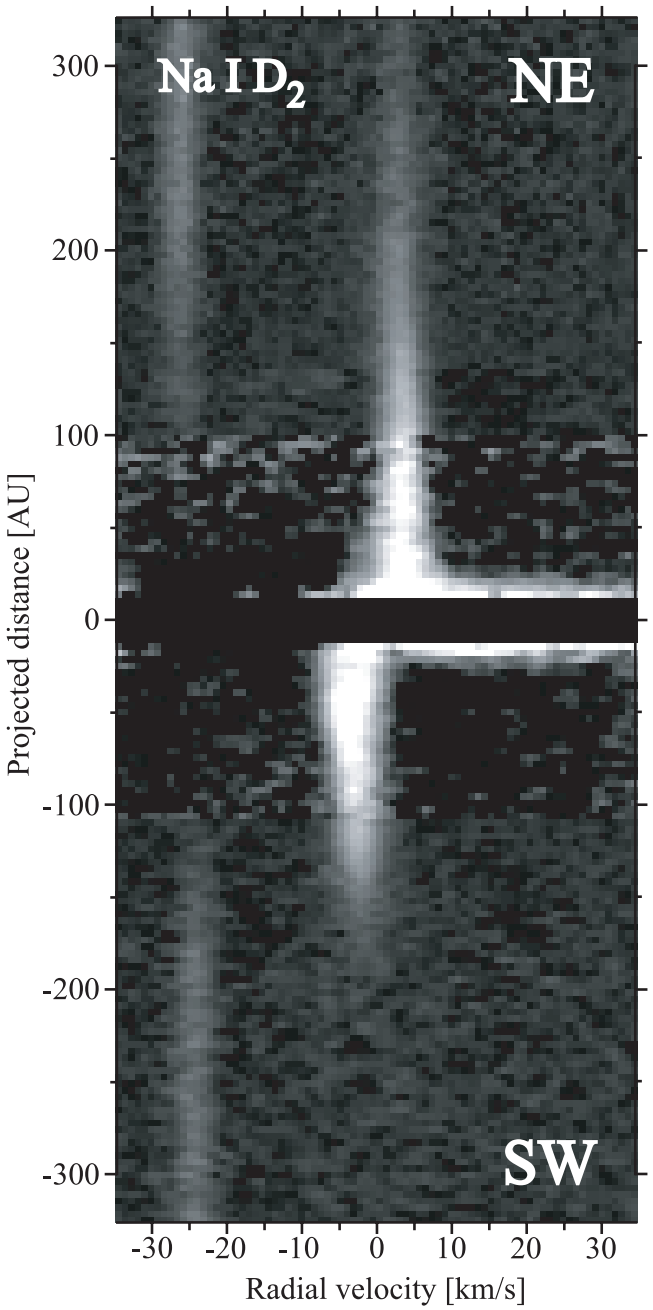

Fig. 2. Na D$_2$ (λ_{air} = 5889.951 Å) emission from the β Pic disk, as seen through four slits parallel to the disk (see Fig. 1). The vertical axis is along the spatial direction, with positive offsets north-east of the star, while the spectral dispersion is along the horizontal axis, centred on the β Pic rest frame of the Na D$_2$ line. The inner 11 AU, showing mostly residual noise from the PSF subtraction, have been masked out. The velocity shift of the NE and SW side is due to Keplerian rotation of the disk, with the SW rotating towards us (Paper I). The grey scale has been scaled non-linearly with the intensity, in order to bring out the bright disk structure close to the star as well as the faint features at greater distances. The emission in the NE can be traced out to the limits of our observations at 323 AU, while the emission in the SW ends abruptly at 150–200 AU (see also Fig. 3). Close to −25 km s^{-1}, telluric Na D$_2$ emission is seen covering the slit. The relative velocity of the sky emission to β Pic varies slightly between the mosaiced observations due to the orbital motion of the Earth between the epochs.

[2] http://physics.nist.gov

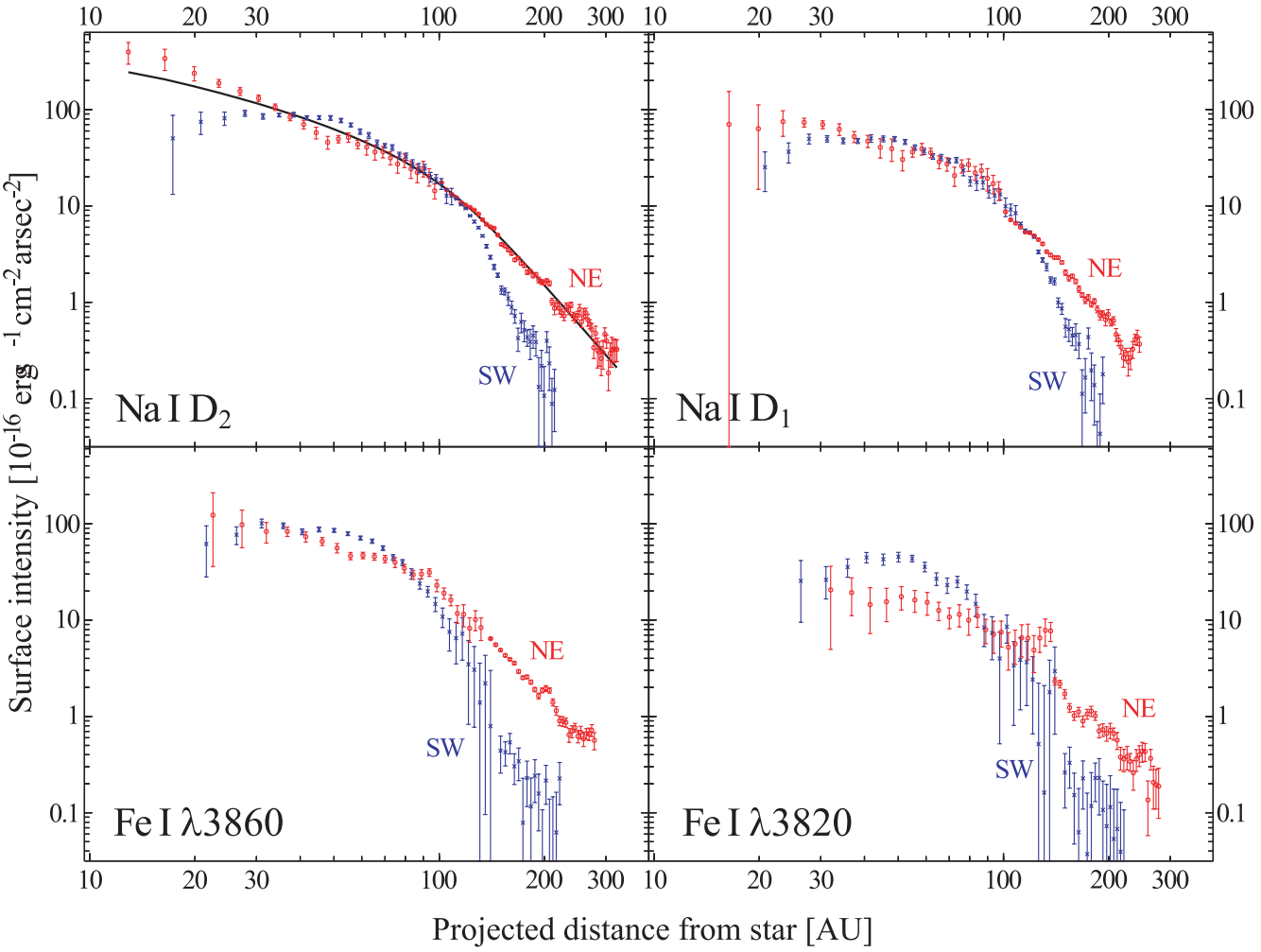

Fig. 3. Determined surface intensity as a function of radial distance in NE and SW for Na D$_{1,2}$ and Fe I λ3859.911, λ3820.425. The fit of Sect. 5.1 is shown for Na I D$_2$ as a an unbroken line. Note the sharp decrease in flux in the SW at 150 AU–200 AU.

Table 2. Selected gas emission lines, 3″ SW in disk.

Line	λ^{a}_{air}	Flux^{b}	σ^{b}_{flux}	E^{c}_{low}	E^{c}_{high}
Fe I	3820.425	61.3	2.5	0.859	4.103
Fe I	3859.911	111.3	3.4	0.000	3.211
Na I D$_2$	5889.951	79.2	4.0	0.000	2.104
Na I D$_1$	5895.924	42.4	2.5	0.000	2.102
Ca II K	3933.663	12.0	1.0	0.000	3.151
Ca II H	3968.468	16.8	1.2	0.000	3.123

[a] Wavelength of transition in air, in units of Å.
[b] Flux in units of 10^{-16} erg s^{-1} cm^{-2} arcsec^{-1}; see Sect. 3.5.
[c] Lower and upper energy levels of transition, in units of eV.

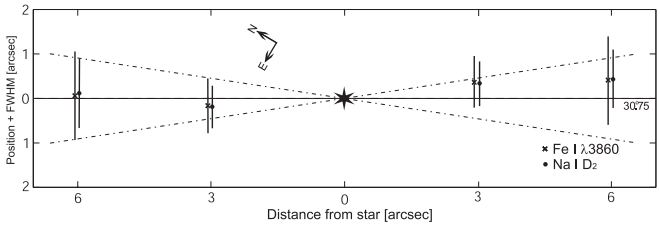

Fig. 4. Measured positions of the Na I and Fe I gas emission relative to the plane at position angle 30.°75. The bars correspond to derived scale heights, obtained by deconvolving the observed height profiles with a Gaussian of 0.″7 *FWHM* simulating the seeing. The inclined dash-dotted lines show the empirical opening angle of the gas disk, corresponding to H/r = 0.28 (see Sect. 5.1). The error in positioning of the slits is on the order of 0.″1.

A very complex height profile is shown by the Ca II H & K lines (Figs. 5 and 6). Especially at 6″ distance from the star, the emission from the disk midplane is much fainter than the emission away from the midplane. In particular, the detected Ca II emission, at 6″ SW of the star, keeps increasing to the limits of the spectroscopic slit 4″ above the disk midplane, meaning that there is a significant number of Ca II ions at 77 AU height above the midplane at 116 AU distance from the star. From Fig. 6 it is evident that the radial velocities of these Ca II ions are small – on the order of a few km s^{-1}. Implications of this fact are discussed in Sect. 5.2.

In order to determine the heliocentric velocity of β Pic accurately, we averaged the heliocentric gas velocities as observed on each side at the distances 3″ and 6″ from the star. In this way, we can assess the system velocity independently from the

Table 3. Radial velocities relative β Pic of ions measured in absorption.

Ion	Δv[a] km s^{-1}	$\sigma_{\Delta v}$[b] km s^{-1}
Fe I	−0.0	0.3
Na I	−1.2	0.3
Ca II[c]	−0.3	2.1
Ti II	0.2	0.8
Ni I	0.4	0.4
Ni II	2.8	3
Cr II	2.2	3

[a] The positive direction is radially away from us, towards β Pic.
[b] Errors are relative only. An additional systematic error of 0.5 km s^{-1} comes from the uncertainty in the system velocity of β Pic.
[c] The radial velocity of Ca II is measured on the infrared lines λ7291.47 and λ7323.89, and not the optically thick Ca II H & K lines.

lines observed in absorption, which are sensitive to possible radial velocities of the absorbers (caused by, e.g., radiation pressure). We determined the heliocentric radial velocity of β Pic to be 20.0 ± 0.5 km s^{-1}, with the error mainly due to the uncertainty in wavelength calibration.

In the spectrum of the star, we measured the absorption profiles corresponding to observed ground state emission lines. Most lines were found to be at, or close to, the system velocity of β Pic (Table 3).

5. Discussion

We proceed by inverting the observations of the projected disk to a radial density law for Na I, and then extend the result by calculating the ionisation structure to find an estimate on the total Na density. By making assumptions of the abundances we construct two models with distinct H densities, test how well the models compare with observations of H I and H_2, and examine how the kinematics of ions in these models are affected by radiation pressure.

5.1. Sodium gas density profile

From the spatial emission profiles we estimate the density distribution of the observed gas by making the following assumptions:

1. The disk is axisymmetric and the density of the emitting medium is well described by

$$n(r,h) = n_0 \left[\left(\frac{r}{r_0}\right)^{2a} + \left(\frac{r}{r_0}\right)^{2b} \right]^{-\frac{1}{2}} \exp\left[-\left(\frac{h}{\alpha r}\right)^2 \right], \quad (1)$$

where r and h are the cylindrical coordinates describing the midplane distance and height over the midplane, respectively, n_0 is a normalising density, r_0 is the broken power-law break distance, a and b are power-law exponents of the inner and outer regions respectively, and α is related to the scale height H of the disk at midplane distance r as $H/r = 2\sqrt{\ln 2}\,\alpha$.
2. The inclination of the disk is close to zero, i.e. we see it edge-on.
3. The emission is optically thin and isotropic.
4. The emitting gas traces the full gas population of that ion.

The observed disk is, of course, not axisymmetric but quite asymmetric in appearance (Figs. 2, 3 and 6). The difference between the NE and SW parts of the inner disk is not that dramatic, though, less than a factor of two in the region where most gas is located (30–120 AU). Thus the assumption of axisymmetry is probably not too bad.

We chose the Na I $D_{1,2}$ lines for the inversion because (A) the S/N is high (~50), (B) the line ratio between D_2 and D_1 is close to 2, implying that the emission is optically thin, and (C) we expect nearly all Na I atoms to be in their ground state (see Sect. 5.3), meaning the resonance $D_{1,2}$ lines trace all of the Na I population. The parameters of Eq. (1) were fitted by constructing a numerical model, simulating observed spatial profiles as a function of the parameters and χ^2-minimising the difference between the model and the observations. In more detail, the model was initiated on a three dimensional grid of height × width × depth dimensions 40 AU × 800 AU × 2000 AU at 1 AU resolution. The central star was assumed to emit 4.5 × 10^{30} erg s^{-1} Å^{-1} at wavelengths close to the Na I D_2 line, and A_{ji} = 6.22 × 10^7 s^{-1} was used as the D_2 transition Einstein coefficient for spontaneous emission, in calculating the scattering cross-section. For each cell, a specific line luminosity was calculated, summed up along the line of sight and geometrically diluted to the distance of the observer at 19.3 pc. This "ideal" image of the disk was then convolved with a Gaussian of $FWHM = 0\farcs7$, simulating the atmospheric seeing, and sampled along the various spectroscopic slit settings of Fig. 1 to fit the observations. In the fit we used the midplane radial emission distribution from 13 AU out to 323 AU of the NE, and the orthogonal profiles at 3″ and 6″ NE of the star. The derived parameters of Eq. (1) for Na I are:

$n_0 = (1.02 \pm 0.04) \times 10^{-5}$ cm^{-3}
$r_0 = 117 \pm 3$ AU
$a = 0.47 \pm 0.06$
$b = 3.16 \pm 0.04$
$H/r = 0.28 \pm 0.05$,

where the quoted errors are 1σ formal fitting errors obtained by making an additional number of fits to artificial data generated by adding random noise, at the estimated noise level, to the observed profile. We have over plotted the Na I fit into Fig. 3.

We can use Eq. (1) with the above parameters to estimate the midplane column density of Na I, to compare with column densities estimated from Na I absorption in the stellar spectrum seen through the disk. If we integrate only over the radii where we are sensitive to Na I emission, that is, from 13 AU out to 323 AU, we obtain a column density of N(Na I) = 3.0×10^{10} cm^{-2}. Extrapolating Eq. (1) to all radii, that is, from zero radius out to infinity, we increase the Na I column density

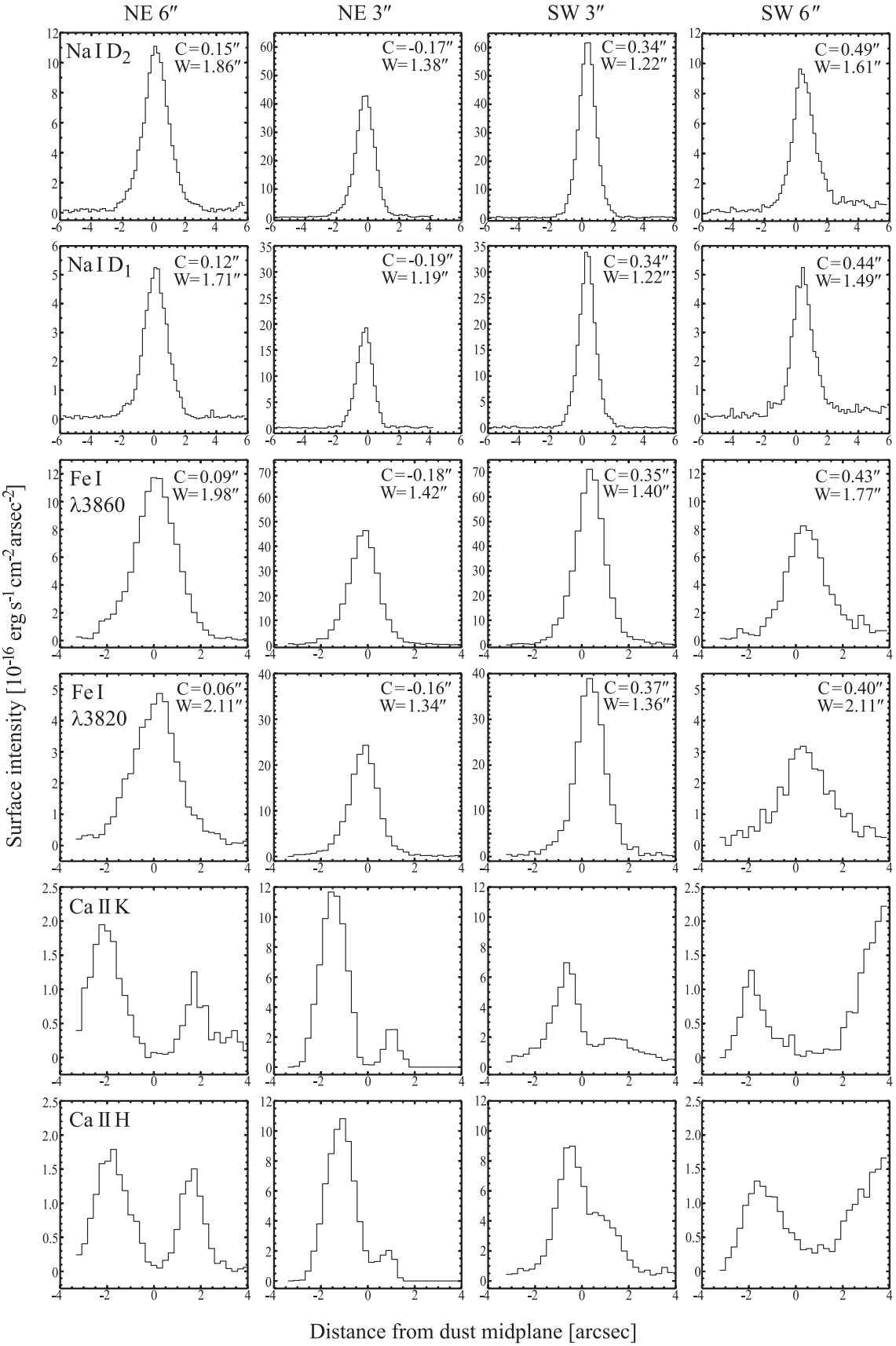

Fig. 5. The flux calibrated vertical profile of the disk gas emission at 3″ and 6″ NE and SW of the star for a few selected lines of Na I, Fe I and Ca II. Zero spatial offset refers to the dust disk midplane defined by the position angle 30.°75 relative to the star, with the positive spatial direction to the north-west (NW). The centre and *FWHM* for Gaussian fits to the profiles are printed in the panels of Gaussian shaped profiles. The SW side dominates the emission at 3″, while the NE side slightly dominates at 6″.

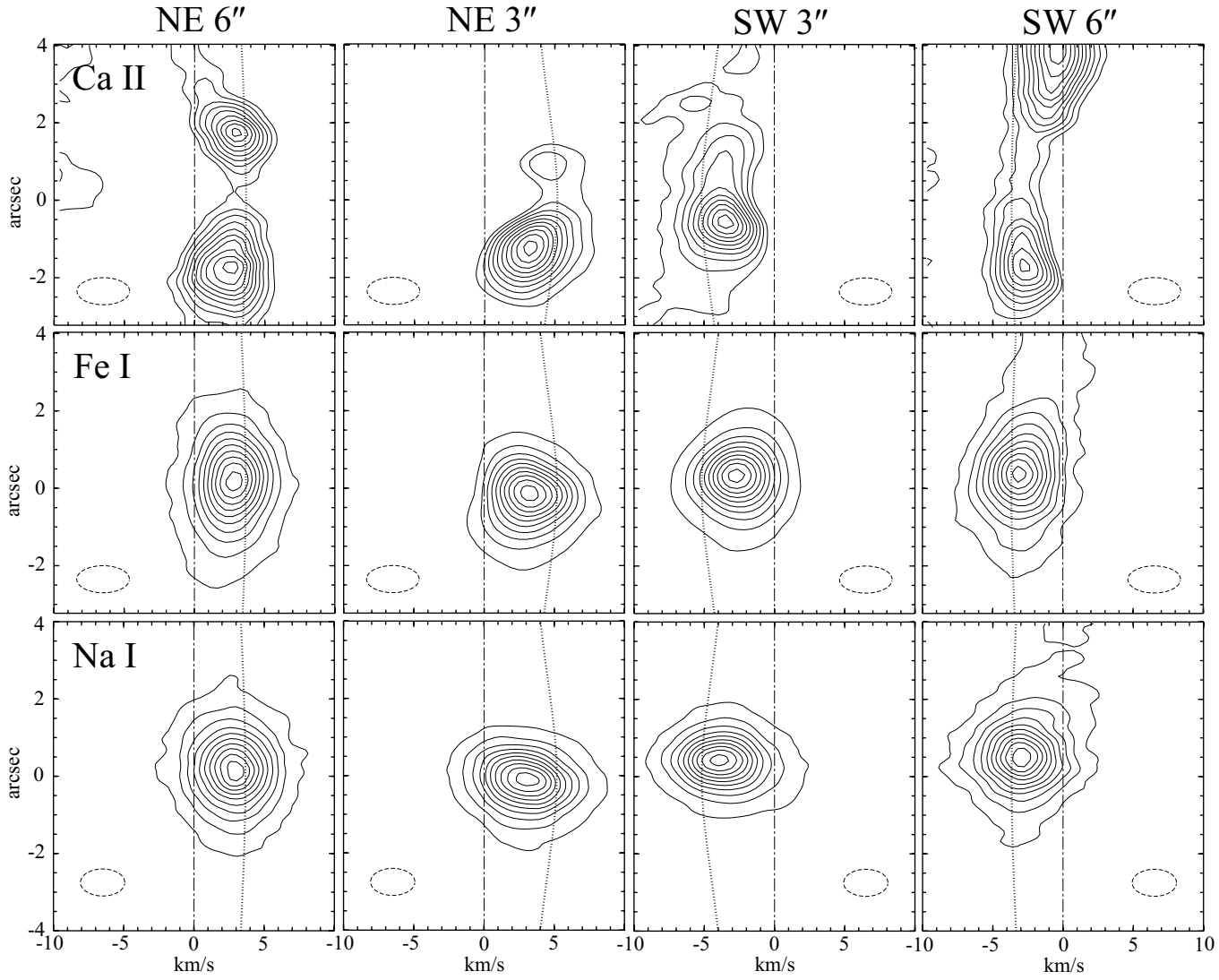

Fig. 6. The velocity distribution of the gas emission as observed by slits orthogonal to the disk at 3″ and 6″ NE and SW of the star for Ca II, Fe I and Na I. To improve the signal to noise, the H & K lines of Ca II, 10 of the brightest Fe I lines, and D_1 and D_2 of Na I were added for each species. The profiles were then normalised so that each level increases one tenth of the peak. The noise in the Fe I and Na I plots is below the lowest level curve, while the lowest level curve for Ca II still shows some noise. Velocities are referred to the system velocity 20.0 km s^{-1} of β Pic, with the positive direction being away from us. Positive offsets in the spatial direction are directed to the north-west (NW). The dash-dotted vertical lines correspond to the system velocity of β Pic, the dotted lines to the Kepler velocity at the projected distance from β Pic (assuming a stellar mass of $M = 1.75\,M_\odot$), while the dashed ellipse in each graph shows the spectral and spatial resolution attained. Note the complexity of the Ca II profile, and how the emission at 6″ SW (right-most panels) can be traced to the limit of the observations. The detected emission profiles from Ni I, Ni II, Ti I, Ti II, Cr I and Cr II are of much lower S/N, but similar to the profiles of Na I and Fe I.

by 40% to $N(\mathrm{Na\,I}) = 4.1 \times 10^{10}\,\mathrm{cm}^{-2}$. This can be compared to our observed column density $N(\mathrm{Na\,I}) = (3.4 \pm 0.4) \times 10^{10}\,\mathrm{cm}^{-2}$. We conclude that most, perhaps all, of the Na I gas seen in absorption is situated in the extended gas disk seen in emission. We have no reason to doubt that originators of other "stable" gas absorption components also belong to this extended disk.

5.2. Radiation pressure

Ions in the β Pic gas disk are subject to appreciable radiation pressure. To evaluate the significance, it is common to define the ratio between the forces of gravitation and radiation, $\beta \equiv F_{\mathrm{rad}}/F_{\mathrm{grav}}$. Since both the radiation and gravitational fields are inversely proportional to the square of the distance to the source, β is constant throughout the β Pic disk. For the observed atoms Na I and Fe I, $\beta \gg 1$, meaning that if left alone, gravity would be largely irrelevant and these atoms would rapidly accelerate out of the system at high velocities. This is not observed (Table 3 and Fig. 6). To investigate what the effects of a braking medium are, we solve the equation of motion for a gas particle,

$$m\frac{\mathrm{d}v}{\mathrm{d}t} = -F_{\mathrm{grav}} + F_{\mathrm{rad}} - F_{\mathrm{fric}}, \tag{2}$$

where F_{fric} is the frictional force. Assuming $F_{\mathrm{fric}} = Cv$, where C is the friction coefficient (proportional to the density of the braking medium), and that the distance an atom travels

before reaching the terminal velocity is much shorter than the size of the disk, Eq. (2) may be solved to yield the terminal velocity (as $t \to \infty$)

$$v_\infty = \frac{\beta - 1}{C} F_{\rm grav}. \quad (3)$$

Equation (2) ignores magnetic forces, which should be of little importance for neutral atoms. If appreciable magnetic fields are present, however, ions with net charges may be significantly affected. We ignore this complication for the moment and assume that the magnetic fields are small enough to play a negligible role for the kinematics of the observed gas particles in the disk.

For β Pic we estimate $\beta_{\rm Na\,I} = 250$ and $\beta_{\rm Fe\,I} = 18$, while C depends on the detailed density and temperature structure. We calculated terminal velocities as a function of radius for the two models of Sects. 5.3.1 and 5.3.2. Details of the solution to Eq. (2), with estimates of C and β for several ions, are found in Liseau (2003).

5.3. Ionisation structure

To estimate the gas density of all Na atoms in the disk, and also get an idea of the total gas density, we need to address the ionisation structure of the disk. We employed the one-dimensional photoionisation/PDR code *Cloudy* (Ferland et al. 1998) for the task. Cloudy consistently maintains the ionization and thermal balance, and solves the radiative transfer by making use of the Sobolev approximation. For a detailed description of the code we used, see Liseau et al. (1999).

Several assumptions have to be made in order to compute the ionisation structure, perhaps the most important being that of the chemical abundances of the atomic gas. Since we have no detailed information, we confine ourselves to study two cases of chemical abundances: solar composition and a strongly metal depleted model. At first we also considered a case with typical interstellar medium abundances, but dismissed it due to the very high degree of Ca depletion compared to solar values, in contradiction with observations. We have no a priori reason to expect any of these assumed abundances to reflect reality, but we believe they still serve as valuable reference cases.

Another important assumption is that of the stellar spectral energy distribution (SED). We assume the atmosphere of β Pic to be well represented by an ATLAS 9 model (Kurucz 1992) with $T_{\rm eff} = 8000$ K, $\log g = 4.5$ (in cm s^{-2}) and $\log(Z/Z_\odot) = 0.0$, and the effective radius to be $R = 1.75\ R_\odot$, implying the luminosity $L = 11\ L_\odot$. Recent VLTI observations of β Pic estimate the stellar radius to be $(1.735 \pm 0.128)\ R_\odot$ (Di Folco et al. 2003), and comparing the ATLAS 9 SED of β Pic with observed data from the HST and FUSE archives, we find the agreement to be generally excellent (see Liseau 2003). Some deviations are found in the far-ultraviolet, where β Pic seems to be a slightly atypical A5V star with possible chromospheric activity (Bouret et al. 2002).

5.3.1. Solar composition disk

Assuming solar abundances throughout the disk, we can fit the radial Na I density of Sect. 5.1 to within 1% by setting the radial density profile of hydrogen nucleii to

$$n({\rm H}) = 2.25 \times 10^3 \left[\left(\frac{r}{r_0} \right)^{2.4} + \left(\frac{r}{r_0} \right)^{5.3} \right]^{-\frac{1}{2}} {\rm cm}^{-3}, \quad (4)$$

where r_0 is the same as in Sect. 5.1. The average fraction of neutral Na in the model is 10^{-3}, while hydrogen is entirely neutral. The hydrogen column densities are $N({\rm H\,I}) = 8 \times 10^{18}$ cm^{-2} and $N({\rm H_2}) = 3 \times 10^{18}$ cm^{-2}, consistent with the observational upper limits of $N({\rm H\,I}) \lesssim$ a few $\times 10^{19}$ cm^{-2} (Freudling et al. 1995) and $N({\rm H_2}) \lesssim 3 \times 10^{18}$ cm^{-2} (3σ, Lecavelier des Etangs et al. 2001). The gas temperature of the model disk is low, $T_{\rm gas}(100\,{\rm AU}) = 13$ K, while the dust is significantly warmer, $T_{\rm dust}(100\,{\rm AU}) = 50$ K. With a radial density as in Eq. (4) and a vertical profile similar to the Na I gas, the total gas disk mass out to 1000 AU becomes $\sim 0.1\ M_\oplus$.

Using the equations of motion of Sect. 5.2 to calculate the terminal velocity of elements subject to the gas drag of the hydrogen density law of Eq. (4) and temperature structure from Cloudy, we find that both Fe and Na, both with $\beta \gg 1$, would reach radial velocities on the order of hundreds to thousands km s^{-1}. That is in clear contradiction with the observed radial velocities reported in Table 3. The purported explanation of Paper I, that Na is ionised most of the time and therefore is subject to a small average radiation pressure, does not apply to Fe; indeed, both Fe I and Fe II experience a radiation pressure with $\beta \gg 1$. We know of only one remaining plausible explanation: there is a braking agent keeping the gas from reaching high velocities.

5.3.2. Metal depleted disk

To investigate the possibility of a more massive disk than implicated by solar abundances of Na I, we impose a radial density profile for hydrogen nucleii,

$$n({\rm H}) = 10^6 \left[\left(\frac{r}{r_0} \right)^{2.4} + \left(\frac{r}{r_0} \right)^{5.4} \right]^{-\frac{1}{2}} {\rm cm}^{-3}, \quad (5)$$

and tune the metal depletion to reproduce the Na I density profile. We found that an overall depletion factor of $\sim 10^{-3}$ (more precisely 8.5×10^{-4}) of the metals with respect to solar composition was required. Due to higher dust-gas interaction, the temperatures of the gas and the dust are similar over the disk, with $T_{\rm gas}(100\,{\rm AU}) = 36$ K and $T_{\rm dust}(100\,{\rm AU}) = 51$ K. The column densities of hydrogen are $N({\rm H\,I}) = 6 \times 10^{20}$ cm^{-2} and $N({\rm H_2}) = 3 \times 10^{21}$ cm^{-2}, significantly higher than the observed upper limits reported by Freudling et al. (1995) and Lecavelier des Etangs et al. (2001). With a radial density as in Eq. (5) and a vertical profile similar to the Na I gas, the total gas disk mass out to 1 000 AU becomes $\sim 40\ M_\oplus$, similar to the mass recently inferred from possible emission in the pure rotational transitions of H_2, $J = 2 \to 0$ (28 μm) and $J = 3 \to 1$ (17 μm), detected from β Pic in ISO/SWS data (Thi et al. 2001). Due to the low gas temperatures of our model, however, the

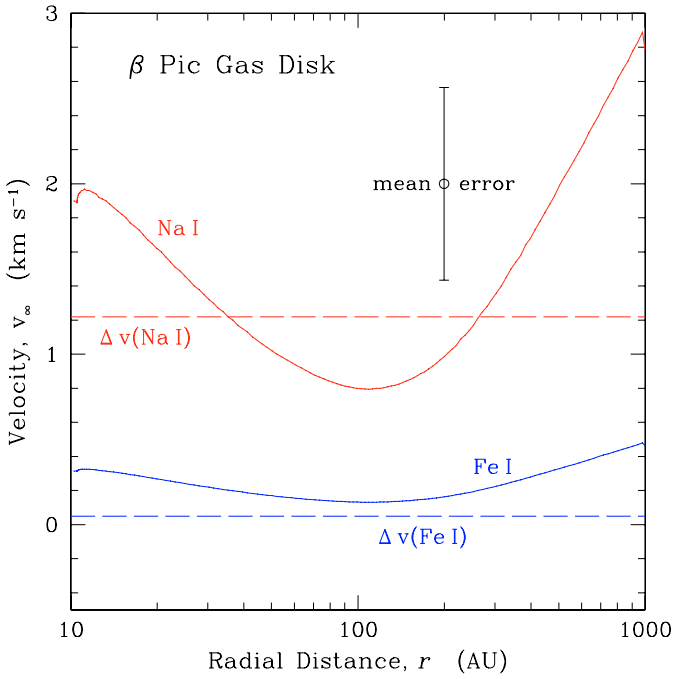

Fig. 7. The terminal velocities for Na I and Fe I in a metal depleted disk with the radial density of Eq. (5), as a function of radius. The horizontal dashed lines show the measured radial velocities, as determined from absorption lines (Table 3), with the estimated error shown by the vertical bar. The error is dominated by the wavelength calibration uncertainty of 0.5 km s^{-1}.

predicted fluxes in the 17 μm and 28 μm lines are only $F_{17} = 6 \times 10^{-15}$ erg s^{-1} cm^{-2} and $F_{28} = 2 \times 10^{-15}$ erg s^{-1} cm^{-2}, respectively, for ortho/para in thermal equilibrium. This is more than an order of magnitude lower than the fluxes $F_{17} = 7.7 \times 10^{-14}$ erg s^{-1} cm^{-2} and $F_{28} = 7.0 \times 10^{-14}$ erg s^{-1} cm^{-2} reported by Thi et al. (2001), and can be traced to their higher assumed gas temperature of 100 K.

Calculating the terminal velocities of the radiation pressure sensitive elements Fe and Na, we produce Fig. 7, where the terminal velocity is plotted against the radial distance. We find that the derived terminal velocities are consistent with observed radial velocities reported in Table 3.

5.4. Summary

We have found that in our thin disk, constructed by fitting a solar composition gas to the Na I observations, the predicted H I and H_2 column densities are consistent with the observed limits. With these low densities, however, the radiation pressure is predicted to accelerate, e.g., Na I to radial velocities inconsistent with observations.

On the other hand, in our thick disk, constructed by fixing the H density to be consistent as the braking agent for the metals, the predicted column densities of H I and H_2 are both above the observed upper limits, although the predicted H_2 *emission* is still far below the claimed detection.

The situation is puzzling, but a possible solution may be found if a main braking agent *different* from hydrogen is in action. If, e.g., the observed gas is replenished from dust collisions rather than being primordial, as seems suggested by the close spatial correlation between gas and dust, then a more natural candidate might be oxygen or oxygen bearing species (P. Artymowicz, private communication). More detailed models are in preparation, but hopefully the upcoming Space InfraRed Telescope Facility will solve the issue unambiguously by better observational constraints.

6. Conclusions

Our main observational results are:

1. We have observed 88 spatially resolved emission lines coming from Fe I, Na I, Ca II, Ni I, Ni II, Ti I, Ti II, Cr I and Cr II in the β Pictoris gas disk.
2. We trace the gas emission to the limits of our observations, from 0.″7 (13 AU) out to 17″ (323 AU) radially to the NE in Na I, and 4″ (77 AU) above the disk plane at radius 6″ (116 AU) in Ca II.
3. The scale height of the gas at 6″ from the star is twice as high as the equivalent dust scale height.
4. There is a brightness NE/SW asymmetry in the gas emission reminiscent of the dust asymmetry, although much stronger.
5. The inner gas disk is tilted by ~5°, similarly to the dust disk.
6. The heliocentric radial velocity of β Pic is 20.0 ± 0.5 km s^{-1}.
7. The radial velocities of ions observed in absorption are close to or at the system velocity of β Pic (to a few km s^{-1}).
8. The estimated radial density from Na I in emission predicts a column density similar to the one observed in absorption, meaning that most, perhaps all, Na I is distributed in the observed disk. We have no reason to doubt that originators of other "stable" gas absorption components also belong to this extended disk.
9. Our disk models show that assuming hydrogen to be the braking agent for metals pushed out by radiation pressure in the β Pic disk leads to contradictions with observations.

A more detailed study of the chemical composition of the β Pic disk will be presented in a forthcoming paper.

Acknowledgements. We would like to thank the staff at the VLT and UVES for their outstanding contributions in performing these demanding service observations, in particular Fernando Comerón for kindly rescheduling an erroneous observation block, and Andrea Modigliani for addressing errors in the UVES pipeline. We acknowledge the interesting discussions we have had with Pawel Artymowicz, Doug Lin, and Philippe Thébault. We thank the referee Alain Lecavelier des Etangs for a rapid and detailed report. This research has made use of NASA's Astrophysics Data System Bibliographic Services, atomic line lists compiled by the National Institute for Standards and Technology, and the SIMBAD database.

References

Artymowicz, P. 2000, Space Sci. Rev., 92, 69
Augereau, J. C., Nelson, R. P., Lagrange, A. M., Papaloizou, J. C. B., & Mouillet, D. 2001, A&A, 370, 447

Aumann, H. H. 1985, PASP, 97, 885
Backman, D. E., & Paresce, F. 1993, in Protostars and Planets III, ed. E. H. Levy, & J. I. Lunine (Tucson: Univ. Arizona Press), 1253
Bouret, J.-C., Deleuil, M., Lanz, T., et al. 2002, A&A, 390, 1049
Di Folco, E., Kervella, P., Thévenin, F., et al. 2003, poster at IAU Symp., 221, Sydney, Australia
Ferland, G. J., Korista, K. T., & Verner, D. A. 1998, PASP, 110, 761
Freudling, W., Lagrange, A. M., Vidal-Madjar, A., Ferlet, R., & Forveille, T. 1995, A&A, 301, 231
Heap, S. R., Lindler, D. J., Lanz, T. M., et al. 2000, ApJ, 539, 435
Hobbs, L. M., Vidal-Madjar, A., Ferlet, R., Albert, C. E., & Gry, C. 1985, ApJ, 293, L29
Holland, W. S., Greaves, J. S., Zuckerman, B., et al. 1998, Nature, 392, 788
Kalas, P., & Jewitt, D. 1995, AJ, 110, 794
Kurucz, R. L. 1992, in The Stellar Populations of Galaxies, ed. B. Barbuy, & A. Renzini (Dordrecht: Kluwer), IAU Symp., 149, 225
Lagrange, A. M., Backman, D. E., & Artymowicz, P. 2000, in Protostars and Planets IV, ed. V. Mannings, A. P. Boss, & S. S. Russell (Tucson: Univ. Arizona Press), 639
Lagrange, A.-M., Beust, H., Mouillet, D., et al. 1998, A&A, 330, 1091
Lecavelier des Etangs, A., Vidal-Madjar, A., Roberge, A., et al. 2001, Nature, 412, 706
Liseau, R. 2003, ESA Special Publication SP-539, in press
Liseau, R., Brandeker, A., Fridlund, M., et al. 2003, A&A, 402, 183
Liseau, R., White, G. J., Larsson, B., et al. 1999, A&A, 344, 342
Mouillet, D., Larwood, J. D., Papaloizou, J. C. B., & Lagrange, A. M. 1997, MNRAS, 292, 896
Olofsson, G., Liseau, R., & Brandeker, A. 2001, ApJ, 563, L77 (Paper I)
Smith, B. A., & Terrile, R. J. 1984, Science, 226, 1421
Thi, W. F., Blake, G. A., van Dishoeck, E. F., et al. 2001, Nature, 409, 60
Weinberger, A. J., Becklin, E. E., & Zuckerman, B. 2003, ApJ, 584, L33
Zuckerman, B. 2001, ARA&A, 39, 549